



Cite this: *Chem. Sci.*, 2025, **16**, 685

All publication charges for this article have been paid for by the Royal Society of Chemistry

Received 28th September 2024
Accepted 15th November 2024

DOI: 10.1039/d4sc06574c
rsc.li/chemical-science

Rare-earth element doped NiFe-MOFs as efficient and robust bifunctional electrocatalysts for both alkaline freshwater and seawater splitting†

Jun Yang, ^{ab} Yong Shen, ^a Jiahui Xian, ^a Runan Xiang^a and Guangqin Li ^{ka}

Based on the target of carbon neutrality, it is very important to explore highly active and durable electrocatalysts for both the hydrogen evolution reaction (HER) and oxygen evolution reaction (OER). Herein, a series of NiFe-based metal–organic frameworks (MOFs) with the doping of various rare-earth elements (Ce, Y, and La) were *in situ* grown on nickel foam by a facile solvothermal process. The representative CeNiFe-MOF showed amazing OER performance with ultralow overpotentials of 224 and 277 mV at 500 mA cm⁻² in 1.0 M KOH and 1.0 M KOH + seawater, respectively. Moreover, it also exhibited favorable activity and durability for both alkaline freshwater and seawater splitting. Theoretical calculations unveiled that Ce doping effectively optimized the adsorption energy of H* and reduced the energy barrier from *OH to *O, thus leading to significant promotion of HER and OER performance. This work provided new inspiration for the electron modulation and activity optimization of MOF-based electrocatalysts.

Introduction

Hydrogen has been regarded as a feasible alternative for conventional fossil fuels due to its appealing energy density and intrinsic carbon-neutral property.^{1–6} Electrocatalytic water splitting, involving the cathodic hydrogen evolution reaction (HER) and anodic oxygen evolution reaction (OER), is believed to be an efficient approach to produce clean hydrogen with high purity.^{6–11} Recently, seawater electrolysis has caught increasing attention in the field of large-scale hydrogen production because seawater accounts for about 96.5% of global water resources.^{5,8,12,13} However, the sluggish kinetics of the HER and OER has seriously hindered the advancement of this promising technology. Pt/C and IrO₂ (RuO₂) are known as the benchmark HER and OER electrocatalysts, respectively, but they suffer from high costs and low reserves, as well as poor durability.^{14–16} Therefore, it is highly desired to develop inexpensive bifunctional electrocatalysts for both freshwater and seawater splitting with high activity and long stability.

Metal–organic frameworks (MOFs), the emerging crystalline materials with abundant sites, versatile functionalities, as well

as tunable structures and electronic properties,^{17–24} have indeed shown fascinating prospects in a variety of electrochemical applications. However, most of the pristine MOFs generally exhibit poor conductivity, and the direct utilization of MOFs as electrocatalysts for the HER and OER still suffers from unsatisfactory activity and stability. A number of efficient methods were reported to promote the electrocatalytic performance of MOFs, such as ligand regulation,^{25–27} element doping,^{28–30} and interface engineering.^{31–33} Rare-earth elements have recently inspired great interest of the scientific community, primarily due to their unique 4f electron structure.^{34–37} With the doping of rare-earth species, not only can the structural properties of MOFs be effectively regulated but abundant electroactive sites can also be constructed, thus resulting in the remarkable optimization of the HER/OER performance. For example, the dysprosium-doped Fe-MOF (Dy_{0.05}Fe-MOF/NF) has been prepared by a simple one-step approach and delivered 100 mA cm⁻² for the OER at a low overpotential of 258 mV.³⁸ The ultrathin Ni-MOF nanosheet arrays doped with yttrium and cerium (NiYCe-MOF/NF) also exhibited outstanding performance for the HER, OER and overall water splitting in alkaline electrolyte.³⁹ Despite the above progress, the MOF-based electrocatalysts have rarely been reported for seawater electrolysis so far. Most importantly, the modulation mechanism of rare-earth doping on the electrochemical performance has remained largely unexplored.

Inspired by the aforementioned regulation strategies, herein, a series of rare-earth element (Ce, Y, and La) doped NiFe-MOFs have been successfully grown on nickel foam (NF) through a facile solvothermal reaction. Benefiting from the

^aMOE Laboratory of Bioinorganic and Synthetic Chemistry, GBRCE for Functional Molecular Engineering, Lehn Institute of Functional Materials, School of Chemistry, Sun Yat-Sen University, Guangzhou 510006, China. E-mail: liuguangqin@mail.sysu.edu.cn

^bSchool of Chemical Engineering, Guangdong University of Petrochemical Technology, Maoming 525000, China

† Electronic supplementary information (ESI) available. See DOI: <https://doi.org/10.1039/d4sc06574c>

‡ These authors contributed equally to this work.



highly exposed sites and fast reaction kinetics, the as-prepared electrocatalysts demonstrated excellent performance in both alkaline freshwater and seawater electrolytes. Specifically, the representative CeNiFe-MOF only required low overpotentials of 113 and 198 mV to achieve current densities of 10 mA cm^{-2} for the HER and 100 mA cm^{-2} for the OER in 1.0 M KOH. Moreover, it can deliver 10 and 100 mA cm^{-2} at low cell voltages of 1.56 and 1.71 V when applied as both the cathode and anode for alkaline freshwater splitting. In 1.0 M KOH + seawater, the CeNiFe-MOF also exhibited a low cell voltage of 1.59 V at 10 mA cm^{-2} and limited activity loss even after long-term operation for 515 h. Furthermore, theoretical calculations were performed to expound the mechanism for performance improvement of CeNiFe-MOF.

Results and discussion

As depicted in Fig. 1a, the CeNiFe-MOF was *in situ* grown on NF by a one-step solvothermal process using $\text{FeCl}_2 \cdot 4\text{H}_2\text{O}$,

$\text{Ce}(\text{NO}_3)_3 \cdot 6\text{H}_2\text{O}$ and terephthalic acid as raw materials. Notably, the NF can not only act as a conductive substrate to support the electrocatalyst but also release Ni^{2+} ions due to the etching of Fe^{3+} ,⁴⁰ which originated from the partial oxidation of Fe^{2+} . The morphologies of the as-prepared samples were first observed by scanning electron microscopy (SEM). It can be seen that both CeNiFe-MOF and NiFe-MOF exhibited the unique coral-like morphology (Fig. 1b and S1†). Transmission electron microscopy (TEM) observation revealed the sheet feature of CeNiFe-MOF (Fig. 1c). Furthermore, the elemental mapping images of CeNiFe-MOF showed the uniform distribution of Ce, Ni and Fe (Fig. 1d-g), which suggested that Ce has been successfully doped into NiFe-MOF.

The X-ray diffraction (XRD) patterns of NiFe-MOF and CeNiFe-MOF in Fig. 2a matched well with that reported for Ni-BDC,⁴¹ confirming the successful growth of these MOFs on NF. This also demonstrated that the incorporation of Ce does not damage the original crystal structure. Additionally, two diffraction peaks derived from the NF substrate emerged at $2\theta = 44.6^\circ$ and 52.0° , which could be attributed to the (111) and (200) crystal planes of metallic Ni. X-ray photoelectron spectroscopy (XPS) measurements were further conducted to investigate the chemical compositions and electronic features of NiFe-MOF and CeNiFe-MOF. The high-resolution Ce 3d scan was deconvoluted into two sets of subpeaks and presented in Fig. S2.† The pair at 885.26 and 904.04 eV corresponded to the $3d_{5/2}$ and $3d_{3/2}$ of Ce^{3+} , whereas the other pairs at 881.95 and 900.78 eV, 887.59 and 906.90 eV, as well as 898.39 and 916.54 eV were associated with Ce^{4+} .^{35,42,43} As displayed in Fig. 2b, the binding energy of Ni 2p for CeNiFe-MOF was higher than that for pristine NiFe-MOF, which suggested that the introduction of Ce could tailor the electronic structure of Ni.^{37,42,44,45} Specifically, the binding energies of $\text{Ni} 2p_{3/2}$ and $\text{Ni} 2p_{1/2}$ for CeNiFe-MOF were identified at 855.98 and 873.66 eV, respectively, in good agreement with those of Ni^{2+} .^{33,46,47} Additionally, two tiny peaks located at 852.71 and 871.57 eV could be attributed to Ni^0 derived from the NF.⁴⁸⁻⁵¹ Fig. 2c exhibits the deconvolution results of high-resolution Fe 2p spectra, where the two peaks at around 710.39 and 723.83 eV were assigned to the $2p_{3/2}$ and $2p_{1/2}$ of Fe^{2+} , while the other pair at binding energies of 712.12 and 725.69 eV corresponded to Fe^{3+} .^{47,52-54} Moreover, two satellite peaks (denoted as "Sat.") were also detected at around 714.72 and 718.84 eV,

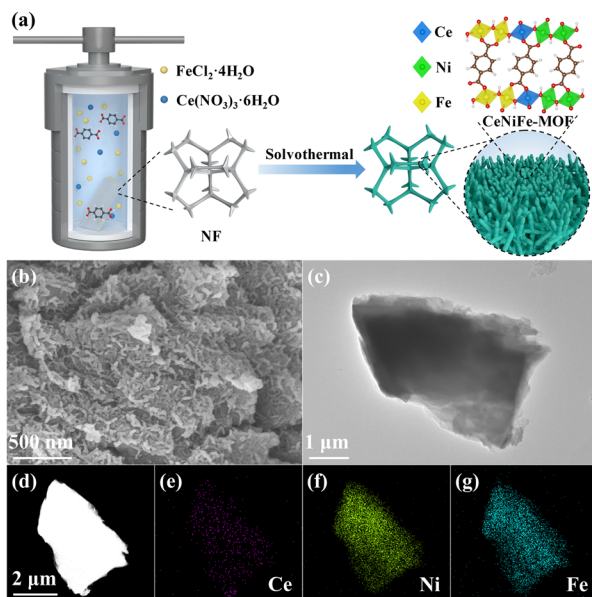


Fig. 1 (a) Schematic synthesis of CeNiFe-MOF on nickel foam. (b) SEM, (c) TEM and (d-g) elemental mapping images of CeNiFe-MOF.

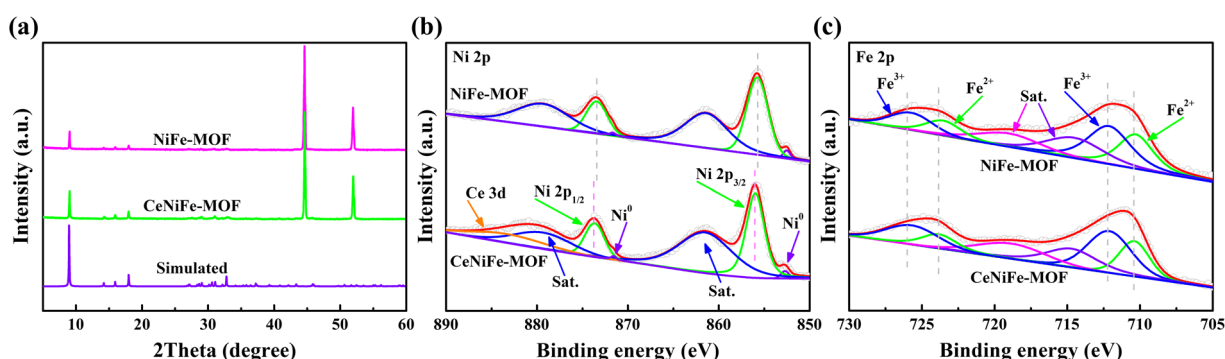


Fig. 2 (a) XRD patterns, (b) Ni 2p and (c) Fe 2p spectra of NiFe-MOF and CeNiFe-MOF.



respectively.^{13,47,55} There was no obvious difference in the position of Fe 2p of these samples, but CeNiFe-MOF was superior in the content of Fe^{3+} to pristine NiFe-MOF (Fig. S3†), indicating that the chemical state of Fe has also been regulated after doping with Ce.^{34,45,56} The above XPS results clearly revealed that the electronic properties of Ni and Fe could be effectively modulated by the introduction of Ce into NiFe-MOF, which is expected to optimize the electrochemical performance of the as-prepared CeNiFe-MOF.

The electrochemical measurements were first conducted in 1.0 M KOH solution by using a typical three-electrode cell. It is found that the CeNiFe-MOF with the $\text{Ce}(\text{NO}_3)_3 \cdot 6\text{H}_2\text{O}$ addition amount of 0.05 mmol showed the best electrocatalytic performance (Fig. S4 and S5†). The content of Ce in this optimal CeNiFe-MOF composite was determined to be 0.59 wt% by

inductively coupled plasma mass spectrometry (ICP-MS). Compared to pristine NiFe-MOF, the HER overpotential of CeNiFe-MOF was more close to that of commercial Pt/C (Fig. 3a and S6†). Specifically, CeNiFe-MOF exhibited a relatively lower value of 113 mV at 10 mA cm⁻² than NiFe-MOF (151 mV), suggesting that the introduction of Ce is beneficial for the improvement of HER activity. The Tafel slope of 59.4 mV dec⁻¹ was observed for CeNiFe-MOF (Fig. 3b), which was much lower than that of pristine NiFe-MOF (71.3 mV dec⁻¹). This smaller Tafel slope is indicative of the superior reaction rates of CeNiFe-MOF for the HER with the Volmer–Heyrovsky mechanism.^{3,19,57,58} As exhibited in Fig. 3c, the self-supporting CeNiFe-MOF electrode also delivered favorable OER activity with an overpotential of only 198 mV at 100 mA cm⁻², which was 50, 96 and 160 mV lower than those of pristine NiFe-MOF (248 mV),

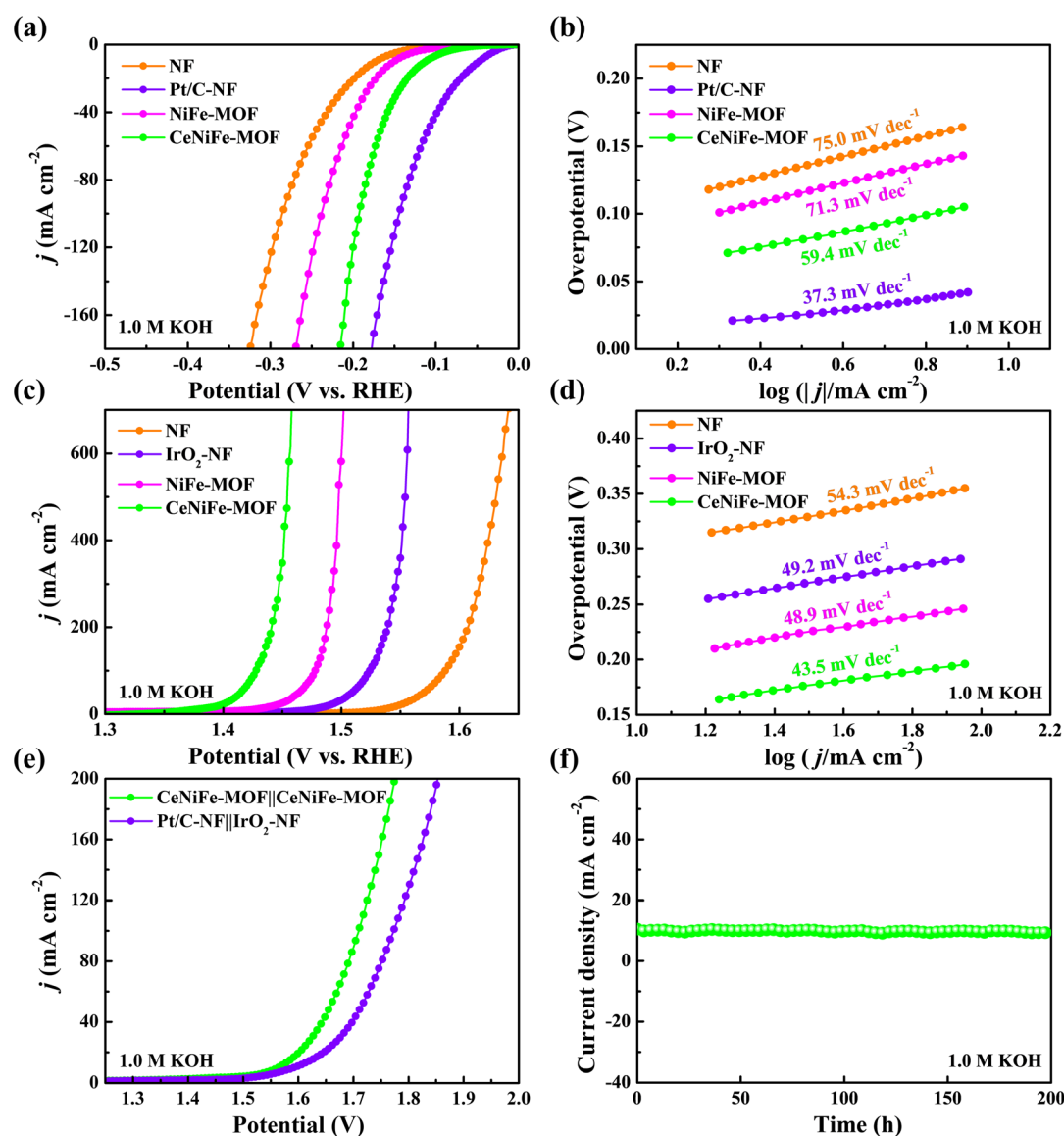


Fig. 3 Electrochemical performance of the samples in 1.0 M KOH. (a) HER polarization curves and (b) the corresponding Tafel slopes. (c) OER polarization curves and (d) the corresponding Tafel slopes. (e) Polarization curves of CeNiFe-MOF||CeNiFe-MOF and Pt/C||IrO₂-NF for water electrolysis. (f) Chronoamperometry curve of CeNiFe-MOF||CeNiFe-MOF toward overall water splitting.



commercial IrO_2 (294 mV) and bare NF (358 mV), respectively. More strikingly, CeNiFe-MOF only required ultralow overpotentials of 224 and 228 mV to drive the large current densities of 500 and 700 mA cm^{-2} (Fig. S7†), demonstrating bright prospects for practical applications. In Fig. 3d, the Tafel slopes of CeNiFe-MOF, NiFe-MOF, IrO_2 and NF were seen to be 43.5, 48.9, 49.2 and 54.3 mV dec^{-1} , respectively, which indicated the fastest electrocatalytic kinetics of CeNiFe-MOF toward the OER.^{19,47,58-60}

To better elucidate the improved electrocatalytic activity of CeNiFe-MOF for both the HER and OER, the electrochemically active surface area (ECSA) was then estimated by the double-layer capacitance (C_{dl}) (Fig. S8†). The C_{dl} of CeNiFe-MOF (1.0 mF cm^{-2}) is larger than those of pristine NiFe-MOF (0.84 mF cm^{-2}) and bare NF (0.51 mF cm^{-2}), indicating that CeNiFe-MOF has more available sites for the efficient HER and OER.^{14,39,60-62} The current density was further normalized by the ECSA (Fig. S9†). CeNiFe-MOF was found to deliver the largest HER current density of $0.39 \text{ mA cm}_{\text{ECSA}}^{-2}$ at an overpotential of 100 mV, in comparison to $0.14 \text{ mA cm}_{\text{ECSA}}^{-2}$ for NiFe-MOF and $0.13 \text{ mA cm}_{\text{ECSA}}^{-2}$ for NF. Moreover, the OER current density of CeNiFe-MOF could reach up to $6.89 \text{ mA cm}_{\text{ECSA}}^{-2}$ at 1.43 V *vs.* RHE, which was approximately 8.2 and 32.8 times higher than those of NiFe-MOF (0.84 $\text{mA cm}_{\text{ECSA}}^{-2}$) and NF (0.21 $\text{mA cm}_{\text{ECSA}}^{-2}$), respectively. These results suggested that CeNiFe-MOF has exceptional intrinsic electrocatalytic HER and OER activity. As seen in Fig. S10,† the CeNiFe-MOF electrocatalyst displayed much smaller charge transfer resistance (R_{ct}) than NiFe-MOF and NF, implying the faster electron transfer during HER and OER processes.^{63,64} The above results revealed that the doping of Ce can not only construct abundant electroactive sites but also accelerate electrocatalytic kinetics, thus remarkably improving the HER and OER performance.

Given the good HER and OER activity, a two-electrode electrolyser assembled with CeNiFe-MOF as both the cathode and anode was further employed to evaluate the capability for overall water splitting. As depicted in Fig. 3e, the cell voltage of CeNiFe-MOF||CeNiFe-MOF (1.56 V) at 10 mA cm^{-2} is lower than that of Pt/C|| IrO_2 (1.59 V). Encouragingly, it required a low cell voltage of merely 1.71 V to drive the high density of 100 mA cm^{-2} , manifesting the excellent activity of CeNiFe-MOF for water electrolysis. CeNiFe-MOF||CeNiFe-MOF can be seen to present considerable stability toward overall water splitting, with a high current retention of 92% even after continuous operation for 200 h (Fig. 3f). The chemical states of CeNiFe-MOF showed very limited changes after a long-term test (Fig. S11†), further indicating its electrocatalytic stability.

The electrochemical properties of as-prepared electrocatalysts were then investigated in simulated seawater electrolyte (1.0 M KOH + 0.5 M NaCl) and alkaline seawater electrolyte (1.0 M KOH + seawater). As compared with pristine NiFe-MOF (Fig. 4a and b), the CeNiFe-MOF required lower overpotentials of 117 and 222 mV in simulated seawater electrolyte to attain current densities of 10 mA cm^{-2} for the HER and 100 mA cm^{-2}

for the OER, respectively. Even at the higher current density of 700 mA cm^{-2} , the required overpotential of CeNiFe-MOF was still as low as 271 mV (Fig. S12†), much better than those of pristine NiFe-MOF (307 mV) and commercial IrO_2 (406 mV). Moreover, the CeNiFe-MOF also exhibited the smaller Tafel slope (Fig. S13†), larger C_{dl} value (Fig. S14†), higher intrinsic activity (Fig. 4c and S15†) and faster charge transfer rate (Fig. S16†) for both the HER and OER, clearly demonstrating its good properties in 1.0 M KOH + 0.5 M NaCl.

Note that the HER activity of CeNiFe-MOF (136 mV@ 10 mA cm^{-2}) in 1.0 M KOH + seawater was significantly higher than that of pristine NiFe-MOF (182 mV@ 10 mA cm^{-2}) and even comparable to that of commercial Pt/C at a large current density (Fig. 4d). Additionally, the CeNiFe-MOF electrocatalyst also exhibited superb performance for the OER in alkaline seawater electrolyte, with the lowest overpotentials of 224, 255 and 277 mV at 100, 300 and 500 mA cm^{-2} , in comparison to 264, 294 and 312 mV for pristine NiFe-MOF, as well as 349, 407 and 433 mV for commercial IrO_2 (Fig. 4e and S17†). It can be seen that the Tafel slopes of CeNiFe-MOF for the HER and OER were much smaller than those of pristine NiFe-MOF (Fig. S18†), which suggested that the Ce doping can effectively accelerate the electrochemical kinetics. The C_{dl} values were further calculated to be 0.45, 0.57 and 0.67 mF cm^{-2} for NF, NiFe-MOF and CeNiFe-MOF, respectively (Fig. S19†), implying more sites in CeNiFe-MOF for alkaline seawater electrolysis.^{7,15,65} As expected, CeNiFe-MOF also displayed the best intrinsic activity in 1.0 M KOH + seawater (Fig. S20†), with the highest HER current density of $1.38 \text{ mA cm}_{\text{ECSA}}^{-2}$ at an overpotential of 150 mV and OER current density of $24.26 \text{ mA cm}_{\text{ECSA}}^{-2}$ at 1.48 V *vs.* RHE (Fig. 4f). Moreover, the much smaller R_{ct} of CeNiFe-MOF (Fig. S21†) could contribute well to the electron transport and thus to performance enhancement.^{6-8,15} As depicted in Fig. 4g, CeNiFe-MOF||CeNiFe-MOF just required a low cell voltage of 1.59 V to achieve a current density of 10 mA cm^{-2} , which is 100 mV smaller than that of Pt/C|| IrO_2 . Impressively, CeNiFe-MOF||CeNiFe-MOF exhibited exceptional durability for electrocatalytic seawater splitting, with limited current fluctuation during long-term operation over 515 h (Fig. 4h). These results demonstrate that the as-prepared CeNiFe-MOF can serve as a robust bifunctional electrocatalyst for highly efficient alkaline seawater electrolysis. Compared with other reported electrocatalysts in recent literature, this bifunctional CeNiFe-MOF exhibited better electrochemical performance for the HER, OER and overall water splitting in both alkaline freshwater and seawater electrolytes (Fig. S22-S27 and Table S1-S6†). It is worth mentioning that this is so far among the best OER electrocatalysts in 1.0 M KOH and 1.0 M KOH + seawater, especially compared to the MOF-based composites.

Density functional theory (DFT) calculations were then conducted to understand the modulation mechanism of Ce doping on the electrocatalytic performance. The optimized calculation models are presented in Fig. S28-S33.† It can be seen that the total density of states (DOS) of CeNiFe-MOF near



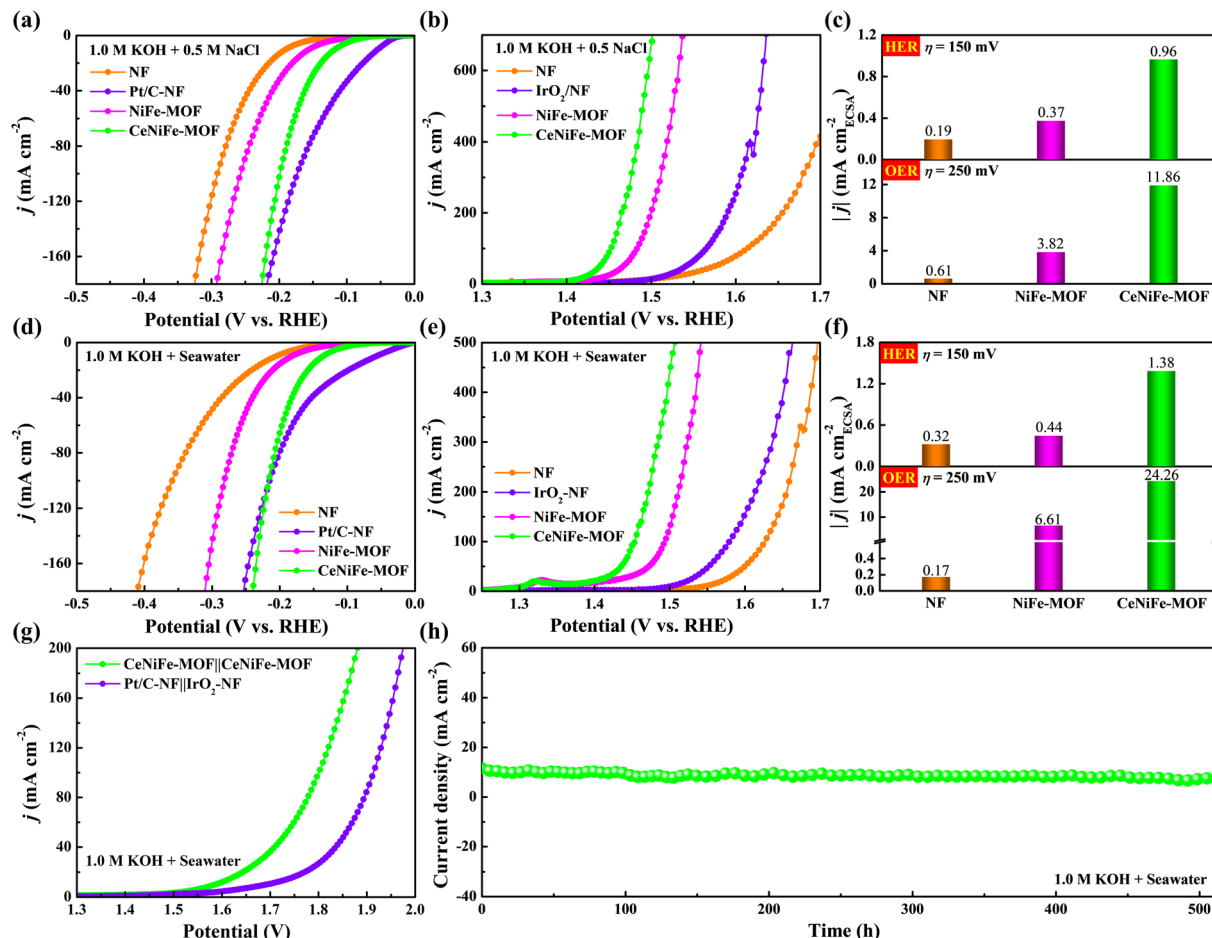


Fig. 4 (a) HER and (b) OER polarization curves of the samples in 1.0 M KOH + 0.5 M NaCl. (c) Comparison of their specific activity in 1.0 M KOH + 0.5 M NaCl. (d) HER and (e) OER polarization curves of the samples in 1.0 M KOH + seawater. (f) Comparison of their specific activity in 1.0 M KOH + seawater. (g) Polarization curves of CeNiFe-MOF||CeNiFe-MOF and Pt/C||IrO₂-NF for alkaline seawater electrolysis. (h) Chronoamperometry curve of CeNiFe-MOF||CeNiFe-MOF toward overall seawater splitting.

the Fermi level was more than that of pristine NiFe-MOF (Fig. 5a), corresponding to the enhanced conductivity and electron transport capability,^{33,66,67} as verified by EIS measurements. Notably, the d-band center of CeNiFe-MOF (−3.09 eV) was much closer to the Fermi level, in comparison to that of NiFe-MOF (−3.47 eV), which indicated the better adsorption of reaction intermediates on active sites.^{66–71} The Gibbs free energy of H* (ΔG_{H^*}) was further calculated to evaluate the HER activity of as-prepared electrocatalysts. As illustrated in Fig. 5b, the Fe in CeNiFe-MOF exhibited the lowest value of ΔG_{H^*} (0.1 eV), which was responsible for the accelerated HER kinetics and the improved HER activity.³⁵ Fig. S34† depicts the free energy for the OER process, where the limiting barrier of Ni in NiFe-MOF was significantly lower than that of Fe in NiFe-MOF and CeNiFe-MOF, suggesting that Ni atoms are the major active sites for the OER. As shown in Fig. 5c, the rate-determining step (RDS) on Ni sites of NiFe-MOF and CeNiFe-MOF is the conversion of OH* to O*. It was found that the energy barrier of RDS decreased from 2.15 to 1.82 eV after incorporating Ce into NiFe-MOF, implying that the introduction of Ce is beneficial to stimulate the OER

process.^{37,72} Additionally, the calculations also manifested that Ce is highly efficient for the electrocatalytic OER but inactive for the HER (Fig. 5d and S35†). The above results demonstrated that Ce doping played a key role in modulating the electronic structure of reaction sites and optimizing the adsorption of intermediates, thus leading to superior HER and OER performance.

To further demonstrate the universality of this doping engineering for performance boost, other rare-earth elements such as Y and La were also introduced into NiFe-MOF to prepare the self-supporting YNiFe-MOF and LaNiFe-MOF electrodes. XRD measurements confirmed their successful preparation (Fig. S36†). As expected, YNiFe-MOF and LaNiFe-MOF were found to exhibit enhanced electrocatalytic properties for both the HER and OER in different electrolytes, including lower reaction overpotentials, smaller Tafel slopes, larger C_{dl} values, higher specific activity and faster charge transport (Fig. S37–S44†), which further indicated the important role of rare-earth doping in performance optimization.

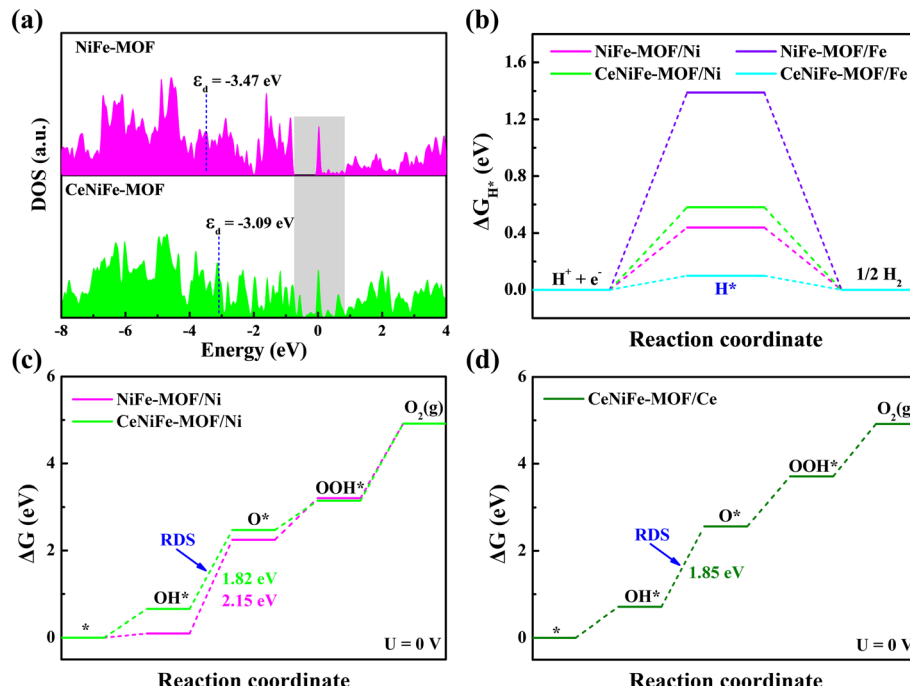


Fig. 5 (a) The DOS of NiFe-MOF and CeNiFe-MOF. (b) The free energy diagram for the HER process. (c and d) The free energy diagrams for the OER process on Ni and Ce sites.

Conclusions

In summary, rare-earth element doped NiFe-MOFs were proposed to be efficient bifunctional electrocatalysts for both the HER and OER in alkaline freshwater and seawater electrolytes. The self-supporting CeNiFe-MOF electrodes presented excellent electrocatalytic capacity in 1.0 M KOH, with a low overpotential of 113 mV at 10 mA cm⁻² for the HER and 198 mV at 100 mA cm⁻² for the OER. Furthermore, it only required low cell voltages of 1.56 and 1.71 V to deliver 10 and 100 mA cm⁻² for alkaline freshwater electrolysis. This CeNiFe-MOF also exhibited outstanding activity (1.59 V@10 mA cm⁻²) and amazing stability (515 h) in 1.0 M KOH + seawater. DFT calculations revealed that the introduction of Ce regulated the electronic structure of active sites and optimized the binding strength of reaction intermediates, thus significantly accelerating the HER/OER process. Compared to pristine NiFe-MOF, the YNiFe-MOF and LaNiFe-MOF also demonstrated much improved electrocatalytic performance in 1.0 M KOH and 1.0 M KOH + seawater. This simple and effective rare-earth doping strategy can be widely exploited for the design and construction of high-performance electrocatalysts for both alkaline freshwater and seawater splitting.

Data availability

The data that support the findings of this study are available from the corresponding author upon reasonable request.

Author contributions

J. Y. and G. L. designed the project. J. Y. performed all the experiments including synthesis, characterization and electrochemical test. Y. S. conducted theoretical calculations and analyses. J. X. and R. X. carried out the SEM and TEM measurements. G. L. supervised the project. All authors discussed the results and contributed to the preparation of the manuscript.

Conflicts of interest

There are no conflicts to declare.

Acknowledgements

This work was supported by the Overseas High-level Talents Plan of China and the NSFC Projects (22375223 and 22075321). J. Y. would like to thank the Young Innovative Talents Projects in Ordinary Universities in Guangdong Province (2024KQNCX113).

Notes and references

- 1 L. Miao, W. Jia, X. Cao and L. Jiao, *Chem. Soc. Rev.*, 2024, **53**, 2771–2807.
- 2 J. Du, F. Li and L. C. Sun, *Chem. Soc. Rev.*, 2021, **50**, 2663–2695.



3 Y. Wang, S. Wang, Z. L. Ma, L. T. Yan, X. B. Zhao, Y. Y. Xue, J. M. Huo, X. Yuan, S. N. Li and Q. G. Zhai, *Adv. Mater.*, 2022, **34**, 2107488.

4 G. Hai, H. Gao, X. Huang, L. Tan, X. Xue, S. Feng and G. Wang, *Chem. Sci.*, 2022, **13**, 4397–4405.

5 C. P. Wang, Y. X. Lin, L. Cui, J. Zhu and X. H. Bu, *Small*, 2023, **19**, 2207342.

6 W. Liu, W. Que, R. Yin, J. Dai, D. Zheng, J. Feng, X. Xu, F. Wu, W. Shi, X. Liu and X. Cao, *Appl. Catal., B*, 2023, **328**, 122488.

7 H. H. You, D. S. Wu, D. H. Si, M. N. Cao, F. F. Sun, H. Zhang, H. M. Wang, T. F. Liu and R. Cao, *J. Am. Chem. Soc.*, 2022, **144**, 9254–9263.

8 Y. Z. Luo, P. Wang, G. X. Zhang, S. S. Wu, Z. S. Chen, H. Ranganathan, S. H. Sun and Z. C. Shi, *Chem. Eng. J.*, 2023, **454**, 140061.

9 S. Shang, W. Li, L. Zhang, S. Liu, Q. Tang, Y. Ding, C. Li, Y. Sun and H. Wu, *Chem. Eng. J.*, 2024, **496**, 154093.

10 X. Hou, C. Yu, T. Ni, S. Zhang, J. Zhou, S. Dai, L. Chu and M. Huang, *Chin. J. Catal.*, 2024, **61**, 192–204.

11 L. Jiao, Y.-X. Zhou and H.-L. Jiang, *Chem. Sci.*, 2016, **7**, 1690–1695.

12 J. X. Guo, Y. Zheng, Z. P. Hu, C. Y. Zheng, J. Mao, K. Du, M. Jaroniec, S. Z. Qiao and T. Ling, *Nat. Energy*, 2023, **8**, 264–272.

13 M. H. Lin, Y. Yang, Y. H. Song, D. G. Guo, L. P. Yang and L. Liu, *Nano Res.*, 2023, **16**, 2094–2101.

14 Y. Zhao, X. F. Lu, Z. P. Wu, Z. Pei, D. Luan and X. W. D. Lou, *Adv. Mater.*, 2023, **35**, 2207888.

15 J. Chen, L. C. Zhang, J. Li, X. He, Y. Y. Zheng, S. J. Sun, X. D. Fang, D. D. Zheng, Y. S. Luo, Y. Wang, J. Zhang, L. S. Xie, Z. W. Cai, Y. T. Sun, A. A. Alshehri, Q. Q. Kong, C. W. Tang and X. P. Sun, *J. Mater. Chem. A*, 2023, **11**, 1116–1122.

16 Y. Bao, H. Ru, Y. Wang, K. Zhang, R. Yu, Q. Wu, A. Yu, D. S. Li, C. Sun and W. Li, *Adv. Funct. Mater.*, 2024, **34**, 2314611.

17 W. Wang, D. Chen, F. Li, X. Xiao and Q. Xu, *Chem*, 2024, **10**, 86–133.

18 W. R. Cheng, H. B. Zhang, D. Y. Luan and X. W. Lou, *Sci. Adv.*, 2021, **7**, eabg2580.

19 F. S. Farahani, M. S. Rahmanifar, A. Noori, M. F. El-Kady, N. Hassani, M. Neek-Amal, R. B. Kaner and M. F. Mousavi, *J. Am. Chem. Soc.*, 2022, **144**, 3411–3428.

20 H. An, Y. Hu, N. Song, T. Mu, S. Bai, Y. Peng, L. Liu and Y. Tang, *Chem. Sci.*, 2022, **13**, 3035–3044.

21 W. Yang, Q. Liu, J. Yang, J. Xian, Y. Li, G. Li and C.-Y. Su, *CCS Chem.*, 2022, **4**, 2276–2285.

22 H. Wang, X. Liu, Y. Zhao, Z. Sun, Y. Lin, T. Yao and H.-L. Jiang, *Natl. Sci. Rev.*, 2024, **11**, nwae252.

23 Y. Peng, S. Sanati, A. Morsali and H. García, *Angew. Chem., Int. Ed.*, 2023, **62**, e202214707.

24 C. Li, W. Zhang, Y. Cao, J.-Y. Ji, Z.-C. Li, X. Han, H. Gu, P. Braunstein and J.-P. Lang, *Adv. Sci.*, 2024, **11**, 2401780.

25 Z. Q. Xue, K. Liu, Q. L. Liu, Y. L. Li, M. R. Li, C. Y. Su, N. Ogihara, H. Kobayashi, H. Kitagawa, M. Liu and G. Q. Li, *Nat. Commun.*, 2019, **10**, 5048.

26 Q. L. Qi, J. Tai, J. Hu, Z. H. Zhang, L. Q. Dai, H. C. A. Song, M. H. Shao, C. X. Zhang and L. B. Zhang, *ChemCatChem*, 2021, **13**, 4976–4984.

27 Y. X. Kong, C. X. Lu, J. Wang, S. L. Ying, T. Liu, X. H. Ma and F. Y. Yi, *Inorg. Chem.*, 2022, **61**, 10934–10941.

28 X. J. Zhai, Q. P. Yu, G. S. Liu, J. L. Bi, Y. Zhang, J. Q. Chi, J. P. Lai, B. Yang and L. Wang, *J. Mater. Chem. A*, 2021, **9**, 27424–27433.

29 H. Yu, L. Wang, H. Li, Z. Luo, T. T. Isimjan and X. Yang, *Chem.-Eur. J.*, 2022, **28**, e202201784.

30 F. Hu, D. Yu, W.-J. Zeng, Z.-Y. Lin, S. Han, Y. Sun, H. Wang, J. Ren, S.-F. Hung, L. Li and S. Peng, *Adv. Energy Mater.*, 2023, **13**, 2301224.

31 C. X. Guo, Y. Jiao, Y. Zheng, J. Luo, K. Davey and S. Z. Qiao, *Chem*, 2019, **5**, 2429–2441.

32 M. J. Wang, Y. Xu, C. K. Peng, S. Y. Chen, Y. G. Lin, Z. W. Hu, L. Sun, S. Y. Ding, C. W. Pao, Q. Shao and X. Q. Huang, *J. Am. Chem. Soc.*, 2021, **143**, 16512–16518.

33 L. M. Deng, F. Hu, M. Y. Ma, S. C. Huang, Y. X. Xiong, H. Y. Chen, L. L. Li and S. J. Peng, *Angew. Chem., Int. Ed.*, 2021, **60**, 22276–22282.

34 H. J. Xu, C. F. Shan, X. X. Wu, M. Z. Sun, B. L. Huang, Y. Tang and C. H. Yan, *Energy Environ. Sci.*, 2020, **13**, 2949–2956.

35 F. Zhang, X. Wang, W. W. Han, Y. Qian, L. S. Qiu, Y. He, L. C. Lei and X. W. Zhang, *Adv. Funct. Mater.*, 2023, **33**, 2212381.

36 Y. Zhu, X. Wang, X. H. Zhu, Z. X. Wu, D. S. Zhao, F. Wang, D. M. Sun, Y. W. Tang, H. Li and G. T. Fu, *Small*, 2023, **19**, 2206531.

37 S. Chen, Z. C. Zheng, Q. Y. Li, H. Wan, G. Chen, N. Zhang, X. H. Liu and R. Z. Ma, *J. Mater. Chem. A*, 2023, **11**, 1944–1953.

38 Y. Ma, G. M. Mu, Y. J. Miao, D. M. Lin, C. G. Xu, F. Y. Xie and W. Zeng, *Rare Met.*, 2022, **41**, 844–850.

39 F. J. Li, M. H. Jiang, C. G. Lai, H. F. Xu, K. Y. Zhang and Z. Jin, *Nano Lett.*, 2022, **22**, 7238–7245.

40 W. D. Zhou, Z. Q. Xue, Q. L. Liu, Y. L. Li, J. Q. Hu and G. Q. Li, *ChemSusChem*, 2020, **13**, 5647–5653.

41 S. L. Zhao, Y. Wang, J. C. Dong, C. T. He, H. J. Yin, P. F. An, K. Zhao, X. F. Zhang, C. Gao, L. J. Zhang, J. W. Lv, J. X. Wang, J. Q. Zhang, A. M. Khattak, N. A. Khan, Z. X. Wei, J. Zhang, S. Q. Liu, H. J. Zhao and Z. Y. Tang, *Nat. Energy*, 2016, **1**, 16184.

42 M. J. Liu, K. A. Min, B. Han and L. Y. S. Lee, *Adv. Energy Mater.*, 2021, **11**, 2101281.

43 F. Larachi, J. Pierre, A. Adnot and A. Bernis, *Appl. Surf. Sci.*, 2002, **195**, 236–250.

44 S. Nagappan, A. Karmakar, R. Madhu, H. N. Dhandapani, K. Bera, A. De and S. Kundu, *ACS Appl. Energy Mater.*, 2022, **5**, 12768–12781.

45 Y. Y. Wen, Z. T. Wei, J. H. Liu, R. Li, P. Wang, B. Zhou, X. Zhang, J. Li and Z. X. Li, *J. Energy Chem.*, 2021, **52**, 412–420.

46 C. P. Wang, Y. Feng, H. Sun, Y. R. Wang, J. Yin, Z. P. Yao, X. H. Bu and J. Zhu, *ACS Catal.*, 2021, **11**, 7132–7143.

47 Y. F. Li, W. J. Ma, H. H. Yang, Q. Y. Tian, Q. Xu and B. X. Han, *Chem. Commun.*, 2022, **58**, 6833–6836.

48 J. Hao, J. W. Liu, D. Wu, M. X. Chen, Y. Liang, Q. Wang, L. Wang, X. Z. Fu and J. L. Luo, *Appl. Catal., B*, 2021, **281**, 119510.



49 Y. Yang, H. Q. Yao, Z. H. Yu, S. M. Islam, H. Y. He, M. W. Yuan, Y. H. Yue, K. Xu, W. C. Hao, G. B. Sun, H. F. Li, S. L. Ma, P. Zapol and M. G. Kanatzidis, *J. Am. Chem. Soc.*, 2019, **141**, 10417–10430.

50 Z. Q. Xue, X. Li, Q. L. Liu, M. K. Cai, K. Liu, M. Liu, Z. F. Ke, X. L. Liu and G. Q. Li, *Adv. Mater.*, 2019, **31**, 1900430.

51 X. X. Wu, T. Zhang, J. X. Wei, P. F. Feng, X. B. Yan and Y. Tang, *Nano Res.*, 2020, **13**, 2130–2135.

52 Y. Z. Liu, X. T. Li, Q. D. Sun, Z. L. Wang, W. H. Huang, X. Y. Guo, Z. X. Fan, R. Q. Ye, Y. Zhu, C. C. Chueh, C. L. Chen and Z. L. Zhu, *Small*, 2022, **18**, 2201076.

53 D. S. Raja, C. L. Huang, Y. A. Chen, Y. M. Choi and S. Y. Lu, *Appl. Catal., B*, 2020, **279**, 119375.

54 C. X. Zhang, Q. L. Qi, Y. J. Mei, J. Hu, M. Z. Sun, Y. J. Zhang, B. L. Huang, L. B. Zhang and S. H. Yang, *Adv. Mater.*, 2023, **35**, 2208904.

55 T. Yamashita and P. Hayes, *Appl. Surf. Sci.*, 2008, **254**, 2441–2449.

56 H. J. Xu, B. K. Wang, C. F. Shan, P. X. Xi, W. S. Liu and Y. Tang, *ACS Appl. Mater. Interfaces*, 2018, **10**, 6336–6345.

57 J. Yu, Y. Qian, Q. Wang, C. Su, H. Lee, L. Shang and T. Zhang, *EES Catal.*, 2023, **1**, 571–579.

58 M. Zhao, W. Li, J. Y. Li, W. H. Hu and C. M. Li, *Adv. Sci.*, 2020, **7**, 2001965.

59 S. L. Lyu, C. X. Guo, J. N. Wang, Z. J. Li, B. Yang, L. C. Lei, L. P. Wang, J. P. Xiao, T. Zhang and Y. Hou, *Nat. Commun.*, 2022, **13**, 6171.

60 K. Ge, S. J. Sun, Y. Zhao, K. Yang, S. Wang, Z. H. Zhang, J. Y. Cao, Y. F. Yang, Y. Zhang, M. W. Pan and L. Zhu, *Angew. Chem., Int. Ed.*, 2021, **60**, 12097–12102.

61 F. P. Cheng, X. Y. Peng, L. Z. Hu, B. Yang, Z. J. Li, C. L. Dong, E. L. Chen, L. C. Hsu, L. C. Lei, Q. Zheng, M. Qiu, L. M. Dai and Y. Hou, *Nat. Commun.*, 2022, **13**, 6486.

62 Y. M. Sun, Z. Q. Xue, Q. L. Liu, Y. L. Jia, Y. L. Li, K. Liu, Y. Y. Lin, M. Liu, G. Q. Li and C. Y. Su, *Nat. Commun.*, 2021, **12**, 1369.

63 Y. R. Wang, A. N. Wang, Z. Z. Xue, L. Wang, X. Y. Li and G. M. Wang, *J. Mater. Chem. A*, 2021, **9**, 22597–22602.

64 Y. S. Chen, J. K. Wang, Z. B. Yu, Y. P. Hou, R. H. Jiang, M. Wang, J. Huang, J. H. Chen, Y. Q. Zhang and H. X. Zhu, *Appl. Catal., B*, 2022, **307**, 121151.

65 J. Sun, Z. Zhang and X. Meng, *Appl. Catal., B*, 2023, **331**, 122703.

66 Y. Jiang, T.-Y. Chen, J.-L. Chen, Y. Liu, X. Yuan, J. Yan, Q. Sun, Z. Xu, D. Zhang, X. Wang, C. Meng, X. Guo, L. Ren, L. Liu and R. Y.-Y. Lin, *Adv. Mater.*, 2024, **36**, 2306910.

67 S. Zhang, Z. Huang, T. T. Isimjan, D. Cai and X. Yang, *Appl. Catal., B*, 2024, **343**, 123448.

68 L. Song, L. Guo, J. Mao, Z. Li, J. Zhu, J. Lai, J. Chi and L. Wang, *ACS Catal.*, 2024, **14**, 6981–6991.

69 Q. Hu, K. Gao, X. Wang, H. Zheng, J. Cao, L. Mi, Q. Huo, H. Yang, J. Liu and C. He, *Nat. Commun.*, 2022, **13**, 3958.

70 X. W. Chang, S. Li, L. Wang, L. Dai, Y. P. Wu, X. Q. Wu, Y. Tian, S. Zhang and D. S. Li, *Adv. Funct. Mater.*, 2024, **34**, 2313974.

71 J. Zhou, P. Li, X. Xia, Y. Zhao, Z. Hu, Y. Xie, L. Yang, Y. Liu, Y. Du, Q. Zhou, L. Yu and Y. Yu, *Appl. Catal., B*, 2024, **359**, 124461.

72 F. P. Cheng, Z. J. Li, L. Wang, B. Yang, J. G. Lu, L. C. Lei, T. Y. Ma and Y. Hou, *Mater. Horiz.*, 2021, **8**, 556–564.

